Redox Fluctuations and Organic Complexation Govern Uranium Redistribution from U(IV)-Phosphate Minerals in a Mining-Polluted Wetland Soil, Brittany, France

Lucie Stetten, Pascale Blanchart, Arnaud Mangeret, Pierre Lefebvre, Pierre Le Pape, Jessica Brest, Pauline Merrot, Anthony Julien, Olivier Proux, Samuel Webb, et al.

Redox Fluctuations and Organic Complexation Govern Uranium Redistribution from U(IV)-Phosphate Minerals in a Mining-Polluted Wetland Soil, Brittany, France

Lucie Stetten,[†,‡] Pascale Blanchart,[‡] Arnaud Mangeret,[‡] Pierre Lefebvre,[†] Pierre Le Pape,[†] Jessica Brest,[†] Pauline Merrot,[†] Anthony Julien,[‡] Olivier Proux,[§,∥] Samuel M. Webb,[⊥] John R. Bargar,[⊥] Charlotte Cazala,[‡] and Guillaume Morin*[,†]

[†]Institut de Minéralogie, de Physique des Matériaux et de Cosmochimie (IMPMC), UMR 7590 CNRS-Sorbonne Université-IRD-MNHN, case 115, 4 place Jussieu, 75252 Paris Cedex 5, France

[‡]Institut de Radioprotection et de Sûreté Nucléaire, IRSN, 31 Avenue de la Division Leclerc, 92262 Fontenay-aux-Roses, France

[§]Université Grenoble Alpes, CNRS, IRD Irstea Météo, OSUG, FAME, 38000 Grenoble, France

[∥]BM30B/CRG-FAME, ESRF, Polygone Scientifique Louis Néel, 71 avenue des Martyrs, 38000 Grenoble, France

[⊥]Stanford Synchrotron Radiation Lightsource (SSRL), SLAC National Accelerator National Laboratory, MS 69, 2575 Sand Hill Road, Menlo Park, California 94025, United States

ABSTRACT: Wetlands have been proposed to naturally attenuate U transfers in the environment via U complexation by organic matter and potential U reduction. However, U mobility may depend on the identity of particulate/dissolved uranium source materials and their redox sensitivity. Here, we examined the fate of uranium in a highly contaminated wetland (up to 4500 mg·kg^{-1} U) impacted by former mine water discharges. Bulk U L_{III}-EXAFS and (micro-)XANES combined with SEM-EDXS analyses of undisturbed soil cores show a sharp U redox boundary at the water table, together with a major U redistribution from U(IV)-minerals to U(VI)-organic matter complexes. Above the water table, U is fully oxidized into mono- and bidentate U(VI)-carboxyl and monodentate U(VI)-phosphoryl complexes. Minute amounts of U(VI)-phosphate minerals are also observed. Below the water table, U is fully reduced and is partitioned between U(IV)-phosphate minerals (i.e., ningyoite and a lermontovite-like phase), and bidentate U(IV)-phosphoryl and monodentate U(IV)-carboxyl complexes. Such a U redistribution from U-minerals inherited from mine water discharge deposits could result from redox cycling nearby the water table fluctuation zone. Oxidative dissolution of U(IV)-phosphate minerals could have led to U(VI)-organic matter complexation, followed by subsequent reduction into U(IV)-organic complexes. However, uranium(IV) minerals could have been preserved in permanently waterlogged soil.

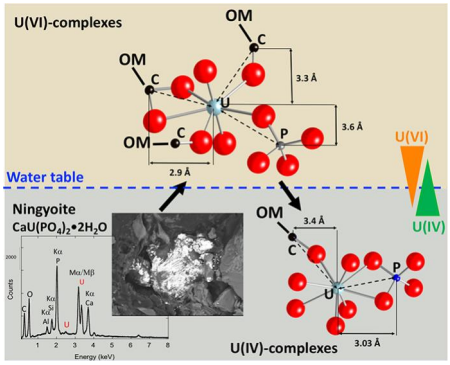

INTRODUCTION

Uranium (U) naturally occurs in soils and sediments at concentrations typically ranging from 1 to 10 mg·kg^{-1}, depending on the bedrock geochemical background.[1,2] However, uranium concentrations may locally exceed these background levels in the vicinity of former uranium mining sites.[3,4] Understanding the processes controlling uranium mobility in such contaminated zones is of prime importance to limit further U transfer to the environment. The mobility of U in soils and sediments is mainly driven by redox processes, ligands complexation, sorption, and precipitation processes.[5,6] In oxic environments, U is mainly present as hexavalent U(VI) and typically occurs as mobile uranyl cation UO_2^{2+} that forms soluble complexes with a wide variety of ligands such as hydroxides, carbonates, and organic moieties.[5,7−9] In reducing environments, U(VI) may be immobilized via biotic[10−12] or abiotic[13−15] reduction into sparingly soluble U(IV) species, such as uraninite UO_2[11,15,16] and U(IV)-phosphate minerals.[17,18] More recently, noncrystalline U(IV) species such as mononuclear U(IV) complexes were observed in laboratory bioassays[18−20] and in a variety of natural reducing environments.[21−25] Such species may be expected to be less stable than crystalline ones under oxidizing[26] and reducing conditions,[21] albeit they were recently discovered in roll-front uranium deposits.[23]

Natural and artificial wetlands such as peats and flooded soils have been recognized for their ability to accumulate U

since they harbor reducing zones.[27−30] However, long-term scavenging of U in such environments may depend on seasonal hydrological fluctuations and organic matter content since these factors play a major role in the control of redox conditions and U mobility.[31−33] Furthermore, investigations of U speciation in peat using chemical extractions have shown significant fraction of sorbed or easily extractable U species, such as 0.1 M bicarbonate extractable U,[34] organically bound (0.1 M $Na_4P_2O_7$) and dilute-acid extractable U.[30,32] Only a few studies have directly addressed the speciation of U in such environments using X-ray absorption spectroscopy (XAS) that allows one to directly determine U oxidation state and molecular level speciation in complex environmental samples. Several of these studies reported U(VI) as being dominant in wetlands and organic-rich soils,[35−37] with U(VI) bound to carboxylic moieties,[37] to additional organophosphates or silicates moieties,[35] or associated with U(VI)-phosphate minerals.[37] In contrast, only a few studies have reported the presence of U(IV) species in peats, such as U(IV) bound to carboxyl moieties[38] or U(IV) coordinated to amorphous Al−P−Fe−Si aggregates,[21,39] these latter favoring U(IV) mobility under colloidal form. Nevertheless, U(IV)-phosphate minerals have not been documented yet in wetlands,[21,37−39] by contrast with lake sediments.[24] Such a variability in the reported U redox state and speciation in peats and wetland soils calls for further investigations to help building conceptual model of U behavior in these putative U retention environments. In addition, U speciation in wetlands may depend on uranium sources, either solid or dissolved, a factor that has not been yet addressed.[21,37−39] It appears thus as primordial to disentangle the factors that govern the evolution of U oxidation state and speciation in wetlands, among which the contaminating sources, the influence of water table fluctuations, and the role of uranium-organic matter interactions.

To fill this knowledge gap, the present study addresses uranium speciation in seasonally saturated soils that are highly contaminated by U due to former mine waters discharges. The chosen site offers the opportunity to evaluate the fate of U(IV)-phosphate minerals that have contaminated this wetland and have then been subjected to seasonal redox fluctuations. Uranium oxidation state and molecular environment were determined using XAS, μ-XAS, and Scanning Electron Microscopy coupled with Energy Dispersive X-ray spectrometry (SEM-EDXS) analyses along two soil core profiles carefully sampled under inert atmosphere in the contaminated wetland.

MATERIALS AND METHODS

Site Description and Sampling. Three soil cores (C1, C2, and C6) were sampled in October 2016 in a seasonally flooded wetland located 300 m downstream from the former *Ty Gallen* uranium mine, Britanny, France. A part of this wooded wetland is severely contaminated with uranium, with topsoil U concentrations reaching 4500 ppm, due to discharges of contaminated mine waters during mining operations that lasted from 1963 to 1981.[4] Cores C2 and C6 were sampled in the wetland, where mine waters collected by the drainage ditch were flowed (Figure SI-S1a of the Supporting Information, SI). The C2 core was sampled in the upstream part of the wetland, 30 m downstream from the mine water outlet. The C6 core was sampled 50 m downstream, in the wettest zone of the wetland (Figure SI-1b). The C1 core, representative of the local geochemical background, was sampled in the east side slope of the wetland topographic depression that was not impacted by the mine water discharges (Figure SI-1b). The cores were extracted using a steel hand corer equipped with 30 cm length PVC core tubes of 5 cm in diameter. Pore water pH was 5.7−6.3. Immediately after coring, the tubes were conditioned under anaerobic atmosphere into sealed aluminized plastic bags within a glovebag purged with N_2. They were then transported in a cool box at ∼4 °C to the IMPMC laboratory within the next 48 h. In an anaerobic glovebox (<20 ppm of O_2), the core tubes were longitudinally cut into two half and 1 cm thick samples were extracted every 5 cm along the soil cores and vacuum-dried in the glovebox. In addition, undisturbed 5 cm length cuts at selected depths were embedded in Norsodyne polyester resin (Gazechim Composites S2010 V) and prepared as polished sections for SEM and μ-XRF/XANES.

Chemical and Mineralogical Analyses. The soil samples were analyzed for total element content at IRSN laboratory after complete acid digestion (see Supporting Information). Majors and trace elements of the digested samples were then measured by inductively coupled plasma-atomic emission spectroscopy (ICP-AES, ICAP 7600 DUO thermoFisher) and inductively coupled plasma- mass spectroscopy (ICP-MS, X7 serie 1 ThermoFisher) respectively. Total carbon contents (TC), Total Organic C (TOC) and Total Inorganic C (TIC) were determined in duplicate using a carbon analyzer (Vario TOC Elementar) equipped with a nondispersive infrared detector. As TIC content was negligible for all samples, TC content could be considered as similar to TOC content. The mineralogical composition of the soil samples was qualitatively determined by X-ray diffraction (XRD) analysis. The XRD powder patterns were collected at the Co Kα-radiation wavelength with an Xpert-Pro Panalytical diffractometer equipped with an X'Celerator solid state detector, counting 2 h per sample over the 5−65° 2θ range, in continuous mode with a 0.017° 2θ step. Uranium-bearing minerals were detected and analyzed by Scanning Electron Microscopy in backscattered electron detection mode coupled with Energy Dispersive X-ray Spectroscopy (SEM-EDXS) using a Zeiss ultra 55 microscope equipped with a Field Emission Gun (FEG) operating at 15 kV with a working distance of 7.5 mm.

XAS Data Collection and Analysis. Uranium L_{III}-edge spectra of the bulk soil samples were recorded at liquid nitrogen temperature in fluorescence detection mode at the 11−2 wiggler-beamline (Stanford Synchrotron Radiation Ligthsource (SSRL)) using a Si(220) double crystal monochromator and a 100 elements Ge array fluorescence detector, and at liquid helium temperature in fluorescence detection mode at the CRG-FAME bending-magnet beamline (European Synchrotron Radiation Facility (ESRF)) using a Si(220) double crystal monochromator and a 30 elements Ge fluorescence detector.[40] The incident beam energy was calibrated by recording the K-edge spectrum of an Y foil in double transmission setup, first inflection point of Y K-edge set to 17038 eV. Data were deadtime corrected and merged using the SIXPACK software,[41] and then energy calibrated, normalized and background subtracted using the ATHENA software[42] to obtain X-ray absorption near edge structure (XANES) and extended X-ray absorption fine structure (EXAFS) spectra. No beam damage was observed after several scans at the same point. Linear combination fitting (LCF) analysis of the XANES and k^3-weighted EXAFS spectra was performed with a custom-built software based on the

Levenberg–Marquardt least-squares minimization algorithm according to procedures detailed in previous studies.[24,25,43] Relevant fitting components were chosen from a large set of U L_{III}-edge model compounds spectra listed in the dedicated section below, based on Principal Component Analysis and Target Transform procedure, as detailed in the SI. Shell-by-shell fitting of the k^3-EXAFS spectra was performed with a custom-built software based on the Levenberg–Marquardt minimization algorithm according to procedures detailed in previous studies.[24,25,43] Selected backscattering phases and amplitude functions used in this procedure were calculated with the FEFF8 code[44] from the crystal structures of torbernite,[45] $CaU(PO_4)_2$[46] and uranyl acetate dihydrate.[47]

μ-XRF and μ-XANES Data Collection and Analysis. Microfocused X-ray fluorescence (μ-XRF) maps were collected at the 2–3 beamline (SSRL). Polished cuts were placed at 45° from the incident beam, and the fluorescence signal was recorded at 17 200 eV using a Vortex silicon drift detector with a beam spot size of $\sim 2 \times 2$ μm^2, step sizes of 10 μm, and a dwell time of 50 ms. Measurements were performed at room temperature with a continuous N_2 flux on the surface of the sample to limit U(IV) oxidation. In the map obtained, several spots of interest were selected for U L_{III}-edge μ-XANES spectroscopy analysis utilizing a Si(111) monochromator calibrated with elemental Y (K-edge at 17038 eV). The spectra were averaged using SIXPACK,[41] energy calibrated, normalized, and analyzed by LCF using ATHENA.[42]

Model Compounds. The U L_{III}-edge XANES and EXAFS data of the soil core samples were interpreted using a large set of model compounds spectra that included natural uraninite UO_{2+x},[11,48] biogenic uraninite,[24] U(IV)-citrate,[24] U(IV)-pyrophosphate,[24] amorphous $CaU(PO_4)_2{\cdot}nH_2O$,[24] uranophane $Ca(UO_2)_2Si_2O_7{\cdot}6H_2O$,[48] U(VI) sorbed to hematite, kaolinite, Illite, chlorite,[48] and amorphous Fe(III)-phosphate,[43] as well as U(VI) biosorbed to microbial cells.[43] Additional model compounds were analyzed at the U L_{III}-edge for the present study and included autunite $Ca(UO_2)_2(PO_4)_2{\cdot}11H_2O$ from the IMPMC collection, U(VI) sorbed to humic acid, synthetic U(IV)-doped rhabdophane and a U(IV)-humus sample that was obtained by experimental incubation of the C2–0 cm humus sample, as described in the SI.

RESULTS AND DISCUSSION

Mineralogical and Chemical Characterization of the Core Profiles. The C2 and C6 cores exhibited a complex alternation of three types of layers separated by diffuse boundaries (Figure SI-2a). The first type of layer, referred to as "humus layer" (O-type layer) was characterized by the quasi absence of crystalline minerals. It typically corresponded to the uppermost sample C2–0 cm and C2–40/45 cm samples, that exhibit a very high TOC in the 27–30 wt % range (Table SI-1, Figure SI-2a). The second type of layer referred to as "organo-mineral layer" (A-type layer) was characterized by the presence of quartz, feldspars, micas, and minor amount of chlorite. This layer exhibited a variable TOC in the 1–25 wt % range. This composition was close to that of the C1 core samples, with a TOC in the 2–25% range, decreasing with depth (Table SI-1, Figure SI-2b), which could be considered as representative of the thick A horizon of local soils that developed over a granitic substratum under a dense deciduous forest cover. In this category, the organic-rich samples, with a high T0C in the 18–25 wt % range (A_1-type layer), included samples C2–5/35 cm (Table SI-1, Figure SI-2a), C6–0/5/15 cm (Table SI-1, Figure SI-2a) and C1–0/5 cm samples (Table SI-1, Figure SI-2b). In the same category, the organic-poor samples with a low TOC in the 1–8 wt % range (A_2-type layer), included the C2–20/25 cm (Table SI-1, Figure SI-2a), C6–20/25/30 cm (Table SI-1, Figure SI-2a), and C1–10/20/30 cm samples (Table SI-1, Figure SI-2b).

The third type of layer referred to as "mine water deposit" was characterized by the presence of a large amount of smectite accompanying quartz, albite, K-feldspars and micas and had a variable TOC in the 0–15 wt % range. This type of layer was well represented in the C2 core by the C2–10/15/30/47/52 cm samples (Table SI-1, Figure SI-2a), and it also occurred with a lower amount of smectite in the C6 core as the C6–10/33/38 cm samples (Table SI-1, Figure SI-2a). It was systematically enriched in uranium (Figure 1), with concentrations ranging between 2000 to 3500 mg/kg in C2 core (Table SI-1, Figure SI-2a), and 500 to 1000 mg/kg in the C6 core (Table SI-1, Figure SI-2a). Such anomalous U concentrations together with the abundance of smectite suggested that this type of layer is representative of weathered granitic material pumped out from the mine and deposited downstream in the wetland by mine water discharges. The accumulation of smectite could be explained by size fractionation of suspended matter during mine water runoff. Hence, uranium-bearing material brought by the mine waters likely enriched in fine clay during its flowing downstream from the mining area and deposited in the weak current zone of the wetland. Accordingly, the higher U content in the mine water deposits of the C2 core than that of the C6 core (Figures 1 and SI-2a; Table SI-1) could be explained by their relative proximity to the mine water outlet (Figure SI-1).

In addition, the A-type soil samples that exhibited smectite were systematically enriched in uranium with concentrations ranging from 1000 mg/kg (C6–0/5 cm), to 2000 mg/kg (C2–25 cm) and up to 4500 mg/kg (C2–5 cm) (Figures 1 and SI-2a, Table SI-1). Such compositions could be partly explained by the mixing of mine water deposits with soil material. Altogether, these observations showed that the superposition of various types of soils layers observed in the C2 and C6 cores likely resulted from successive deposits of soil material interspersed by allochthonous material coming from mine water discharges.

The topsoil organic-rich horizons exhibited high U concentration, i.e., 3000 mg/kg U in the C2–0 cm sample of the O-type. In contrast, at depth, O-type (C2-40/45 cm), A_1-type (C2–35 cm and C6–15 cm) and A_2-type layers (C2–20 cm, C6–20/25/30 cm) exhibited U concentrations in the 9–30 $mg.kg^{-1}$ range, i.e., similar to those in the nonimpacted core C1 (<35 $mg{\cdot}kg^{-1}$), even though they were interposed between U contaminated mine water deposits (Figures 1 and SI-2, Table SI-1). Such contrasted contamination levels in the organic-rich soil layers raised questions about the mechanisms that control U mobility in this heavily contaminated wetland. We have thus investigated the oxidation state and molecular level environment of uranium along the soil cores in order to identify U host phases and retention mechanisms as well as to evaluate the role of redox conditions in the control of U fate.

Evidence for a Uranium Redox Boundary at the Water Table Level. The U L_{III}-edge XANES spectra of bulk samples from the C2 and C6 cores were fit using linear combinations of our U(VI)-humic acid and U(IV)-humus

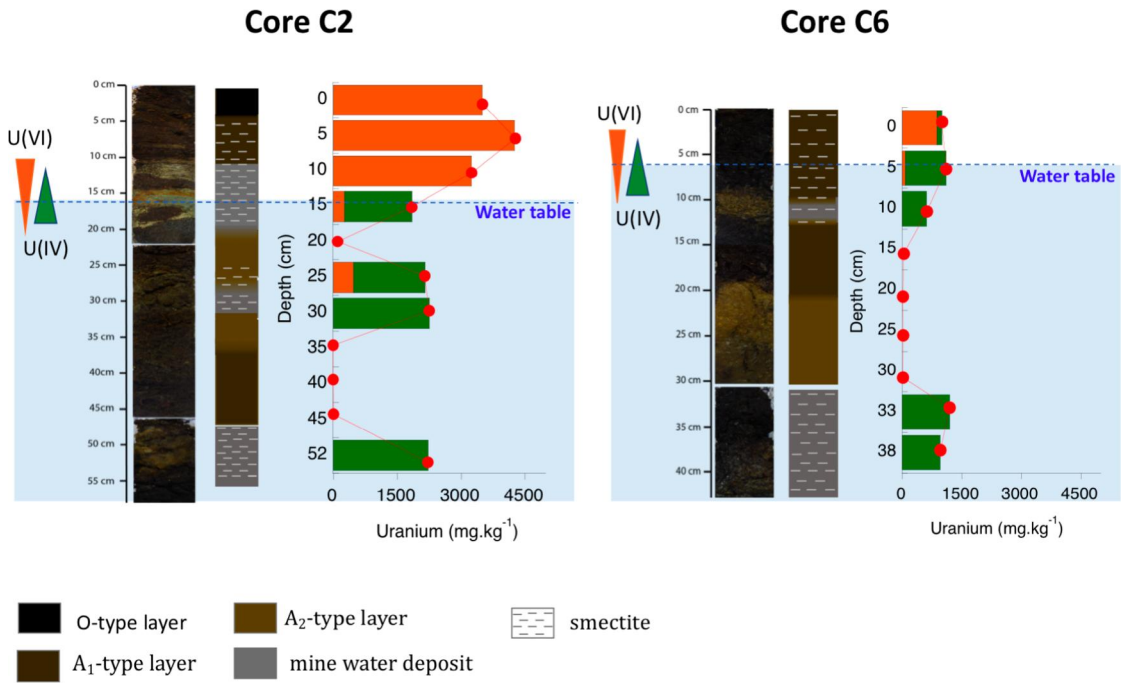

Figure 1. Vertical distribution of bulk uranium concentrations and redox state, and pedo-lithology of the soil cores C2 and C6 sampled in the contaminated wetland. From left to right: picture of the cores, pedo-lithological interpretation based on chemistry and mineralogy data (see Table SI-1; Figure SI-2a and text) and red curve displaying the total bulk uranium concentrations in the solid phase in $mg{\cdot}kg^{-1}$ (see Table SI-1) with bar diagrams displaying the proportions of U(VI) in orange and U(IV) in green obtained from LCF analysis of the U L_{III}-edge XANES data (see Table SI-2 and Figure SI-4), normalized to bulk U. The water table level at the sampling date is indicated in light blue and dash line. The water table level was observed on the field for the C6 core and inferred from the position of the iron-oxide layer for the C2 core (see text).

model compounds spectra (Figure SI-4; Table SI-2). Fitting results obtained with other U(IV) and U(VI) model compounds were similar within a ± 10% deviation. This LCF-XANES analysis indicated the presence of a sharp U(VI)/U(IV) redox boundary, which occurred deeper in the C2 core (10−15 cm) than in the C6 core (0−5 cm) (Figure 1; Figure SI-4; Table SI-2). In the C2 core, uranium was present as 100% U(VI) down to 10 cm, while it was 86−78% U(IV) at 15 and 25 cm depth, and 100% U(IV) below 25 cm (Figure 1; Table SI-2). In the C6 core, uranium was almost 100% U(VI) in the upper layer, while it was 93% as U(IV) at 5 cm and 100% of U(IV) in deeper samples (Figure 1; Table SI-2). This difference could be explained by the distinct topographic elevation of the two coring points with respect to the water table level (Figure 1). In the C2 core sampled upstream in the wetland, the U(VI)/U(IV) redox boundary at 10−15 cm was consistent with the presence of a Fe-rich brown layer (Figures 1 and SI-2a), likely consisting of iron-oxyhydroxides precipitated from aqueous Fe^{2+},[49] which allowed us to infer the position of the water table in this core to be located at ∼15 cm during the sampling period. The C6 core was sampled in the wettest area of the wetland where the soil was almost water-logged at the sampling date, with a water table at ∼5 cm. In this core, the U(VI)/U(IV) redox boundary was found roughly at the same depth according to XANES analysis (Figures 1 and SI-1), i.e., shallower than in the C2 core. These results showed that the depth of the U(VI)/U(IV) redox boundary was mainly controlled by the soil flooding level, below which the establishment of reducing conditions is propitious to U reduction, independently of the type of layers.

In addition, in both cores, the highest U concentrations were found in organic-rich layers of the A1-type (C2−5 cm and C6−5 cm samples) located within the water table fluctuation zone, independently of the oxidation state of U. This observation raises questions about possible U transfers between mine water deposits and neighboring organic-rich soil layers, especially if seasonal fluctuations of the water table lead to U redox cycling. In contrast, in deeper soil layers where U was only present as U(IV), organic-rich and organic-poor samples (A1 and A2 layers respectively) exhibited a very low U content (<30 $mg{\cdot}kg^{-1}$). This concentration is similar to the local geochemical background represented by the U concentration of the uncontaminated core C1 (Figure SI-2b), even though these layers were interposed between highly contaminated mine water deposit layers. These observations suggest that U transfers could have been limited in these reduced layers, compared to the oxidized ones. In order to evaluate such hypotheses and to better understand the mechanisms of putative U remobilization, we have determined the molecular environment of U(VI) and U(IV) species especially across the redox boundary, using EXAFS spectroscopy, μ-XRF, μ-XANES, and SEM analyses.

U(VI) Speciation in the Organic Rich Samples above the Water Table. U(VI) was mainly present as noncrystalline species in the organic-rich C2−0 cm, C2−5 cm, and C6−0 cm samples (Figure 2), the best EXAFS LCF being obtained with 37 to 48% of U(VI)-humic acid and 45 to 63% of U(VI)-biosorbed (Table SI-3). Shell-by-shell fit of the humus layer sample data, C2−0 cm, and A1-type layer sample data, C6−0 cm, confirmed this result, revealing contributions from U−C paths at 2.9 and 3.3 Å, and a U−P path at 3.6 Å (Table SI-4; Figure 3) that we found to be characteristic of the U(VI)-humic acid and U(VI)-biosorbed model compounds spectra. Indeed, shell-by-shell fit of the U(VI)-humic acid model

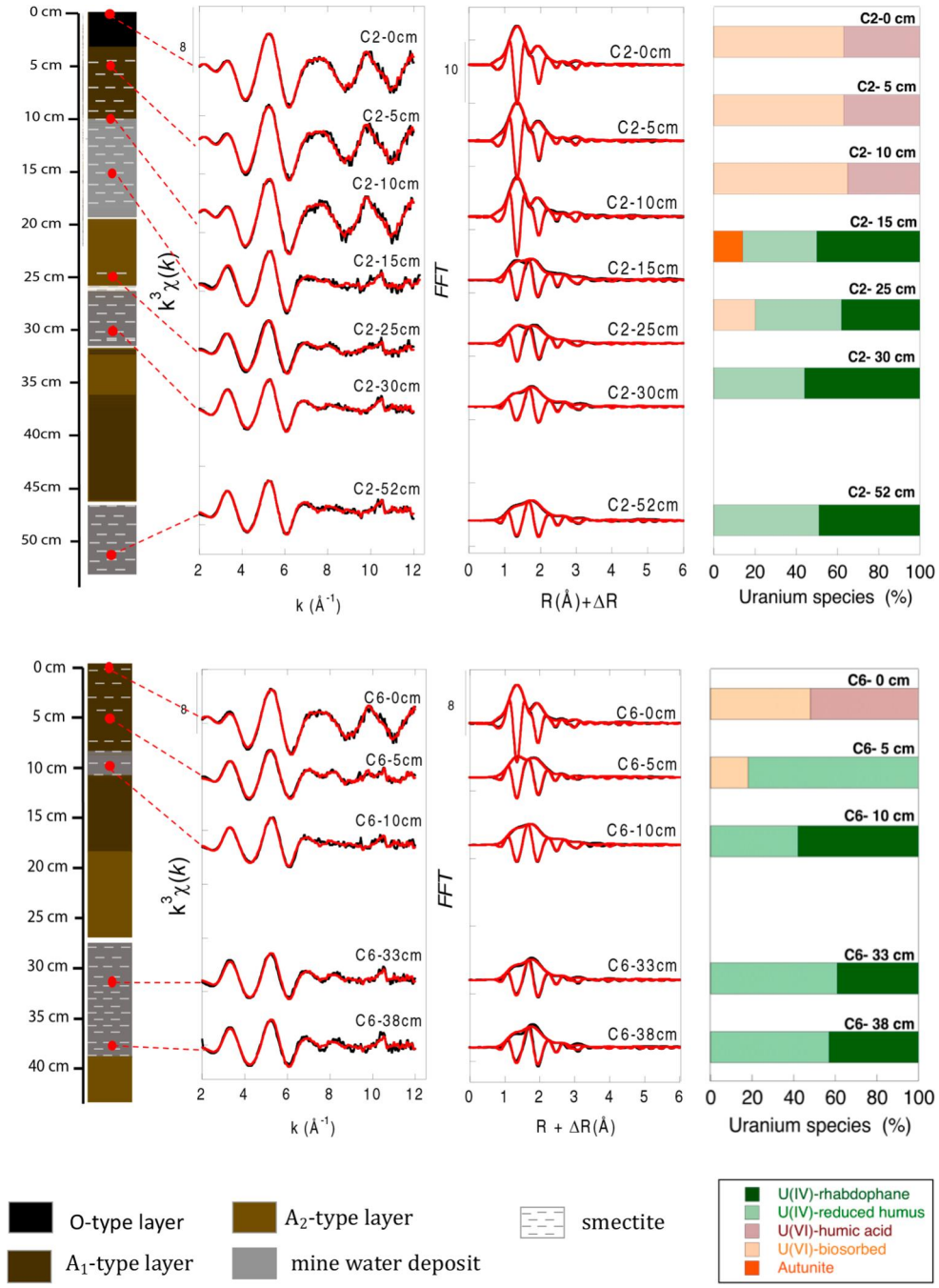

Figure 2. LCF analysis of U L_{III} EXAFS data of C2 and C6 core samples. Experimental and fit curves are displayed in black and red colors, respectively. Modulus and imaginary part of the fast fourier transforms of the experimental and fit curves are also reported. The proportions of the fitting components U(VI)-humic acid (purple), U(VI)-biosorbed (beige), autunite (orange), U(IV)-humus (light green), and U(IV)-rhabdophane (dark green) are normalized to 100%. Non-normalized results and uncertainties are given in Table SI-3. Shell-by-shell analyses of the model compounds spectra are reported in Figures 3, SI-6 and Table SI-4.

compound data (Figures 3 and SI-6) indicated a second neighbor contribution from 2 U−C paths at a distance of 3.3 Å (Table SI-4) that is characteristic of U(VI) bound to carboxyl groups in a monodentate geometry.[47,50] Such geometry was previously proposed for U(VI) complexation to humic substances, based on room-temperature EXAFS analyses.[51,52]

In the U(VI)-humic acid spectrum, we also observed a minor contribution from ∼1 U−C path at 2.9 Å (Figure SI-6; Table SI-4) that we interpret as nonsignificant in this sample. Indeed, Rossberg et al.[54] showed that the number of C atoms fitted at 2.9 Å in the EXAFS spectrum of sorbed uranyl ions was systematically overestimated by ∼1 atom, since this value was obtained by EXAFS in a carbon-free sorption sample. In our U(VI)-biosorbed model compound spectrum,[43] this contribution is significant with ∼2 U−C paths at 2.9 Å (Figures 3 and SI-6; Table SI-4), and could then be attributed to bidentate complexation of U(VI) to ∼1 carboxyl[38,47,50] or carbonate groups,[53] as previously reported by Seder-Colomina et al.[43] In addition, in this model compound, U(VI) is also bound to phosphoryl moieties in a monodentate edge sharing geometry with ∼2 U−P paths at ∼3.6 Å[43,55] (Figures 3 and SI-6; Table SI-4)

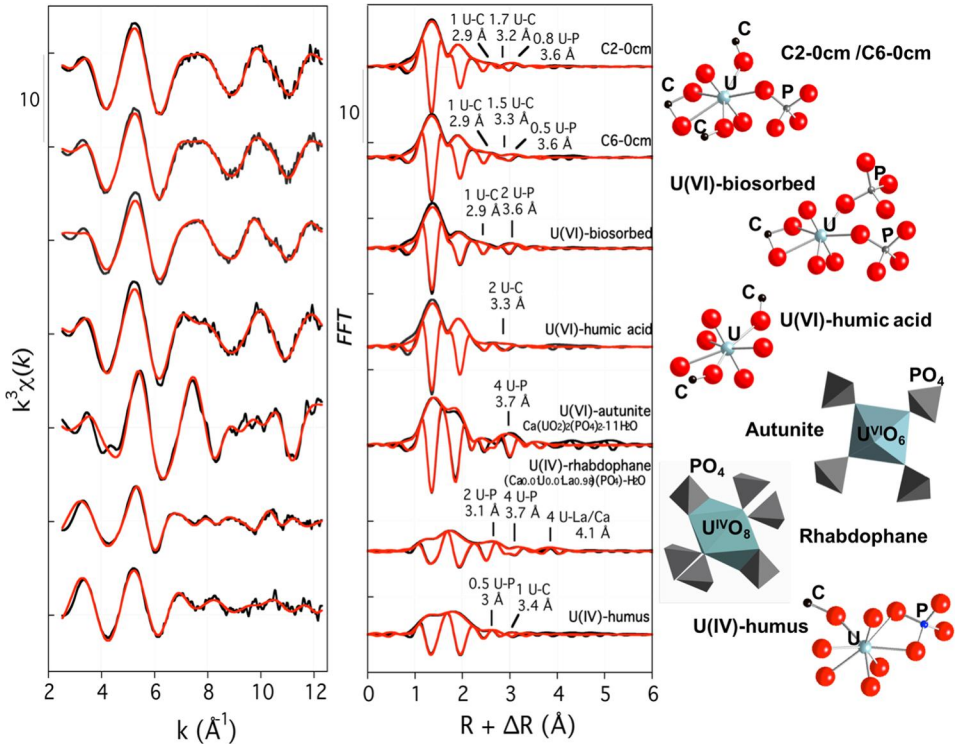

Figure 3. Results of shell-by-shell analysis of U L_{III}-edge EXAFS spectra for soil samples C2−0 cm and C6−0 cm and relevant U(IV) model compounds. Unfiltered k^3-weighted data were fit in k-space (left) and corresponding Fast Fourier Transforms magnitude and imaginary parts are displayed (FFT). Experimental and fit curves are drawn in black and red lines, respectively. Fitting parameters are reported in Table SI-4. In the figure, the N value for the U−C path at 2.9 Å is subtracted by 1 compared to the fitted value reported in Table SI-4 (see text). Detailed fits showing second neighbor contributions to the EXAFS are given in Figure SI-6. A schematic local molecular structure around the U atom, consistent with the EXAFS results, is displayed for each model compound (right).

Accordingly, the shell-by-shell fit results for the C2−0 cm and C6−0 cm soil samples (Table SI-4), can then be interpreted as corresponding to the following average coordination: ∼1 bidentate C at 2.9 Å, ∼1−2 monodentate C at 3.3 Å and 0.5−1 monodentate P at 3.6 Å, as schematized in Figure 3. These results were consistent with LCF results indicating mixtures of the U(VI)-humic acid and U(VI)-biosorbed spectra for these soil samples (Figure 2 and Table SI-3) and thus showed that, in the U contaminated organic-rich soil layers, U(VI) formed monodentate and bidentate complexes with carboxyl groups and monodentate complexes with phosphoryl groups, of organic and/or biological material (Figure 3; Table SI-4). This finding is partly consistent with two recent EXAFS studies of U speciation in a wetland[37] and a peatland,[38] which proposed U(VI) bidentate-mononuclear binding to carboxyl groups.

Here, EXAFS data collected up to k of 12 Å^{-1} yielded evidence for the presence of monodentate U binding to carboxyl groups of humic substances, both in our U(VI)-humic acid model compound and in the topsoil organic-rich samples. The dominance of this complex over the bidentate one could possibly be related to the high U-loading in our heavily contaminated humus layer (3496 mg/kg) and organic rich soil samples (998−4255 mg/kg) as well as in our U(VI)-humic acid sorption sample (1500 mg/kg) compared to the samples studied by Li et al. (2015) (285 mg/kg) and Mikutta et al. (2016) (335 mg/kg). Finally, additional monodentate U binding to phosphoryl groups of humic substance or microbial biomass with a typical U−P distance of 3.6 Å in these humus and organic-rich soil layers is consistent with the results from a previous study of naturally U-rich wetland soils by Regenpurg et al.[35]

The occurrence of U(VI)-mononuclear organic complexes in the organic-rich upper layers of the soils studied was consistent with μ-XRF mapping and μXANES analyses results (Figure 4), which showed a diffuse distribution of U in the organic-rich horizon at 5−8 cm depth in the C6 core. In contrast, U hot spots were abundant at 8−10 cm, in the organic poor layer contaminated by mine water deposit (C6−10 cm) (Figures 4 and SI-7). In this layer, μ-XANES spectra showed that U is mainly present as U(IV) (Figure 4c, and SI-7c) especially at some hot spots that we could directly identified as ningyoite $CaU(PO_4)_2{\cdot}2H_2O$ by SEM-EDXS analysis (Figure 4a, b). The presence of these phosphate minerals was confirmed and quantified by EXAFS analysis of the bulk samples as detailed below.

U(IV) Speciation in the Mine Water Deposits below the Water Table. U(IV) was mainly present in the form of U(IV)-phosphate minerals and mononuclear U(IV)-organic complexes in the mine water deposits located below the uranium redox boundary, i.e., samples C2−30/52 cm and C6−10/33/38 cm (Figure 2; Table SI-3). Indeed, the best EXAFS-LCF adjustments for these samples were obtained with 37−56% U(IV)-rhabdophane and 44−58% U(IV)-humus. Consistently, the relative contribution of the U(IV)-humus component determined by EXAFS LCF was found to be roughly correlated to the TOC of the samples (Figure 2; Tables SI-1 and SI-3). Moreover, similar fitting components, with the highest proportion of U(IV)-rhabdophane (59%), were determined for the C6−10 cm sample (Figure 2; Table

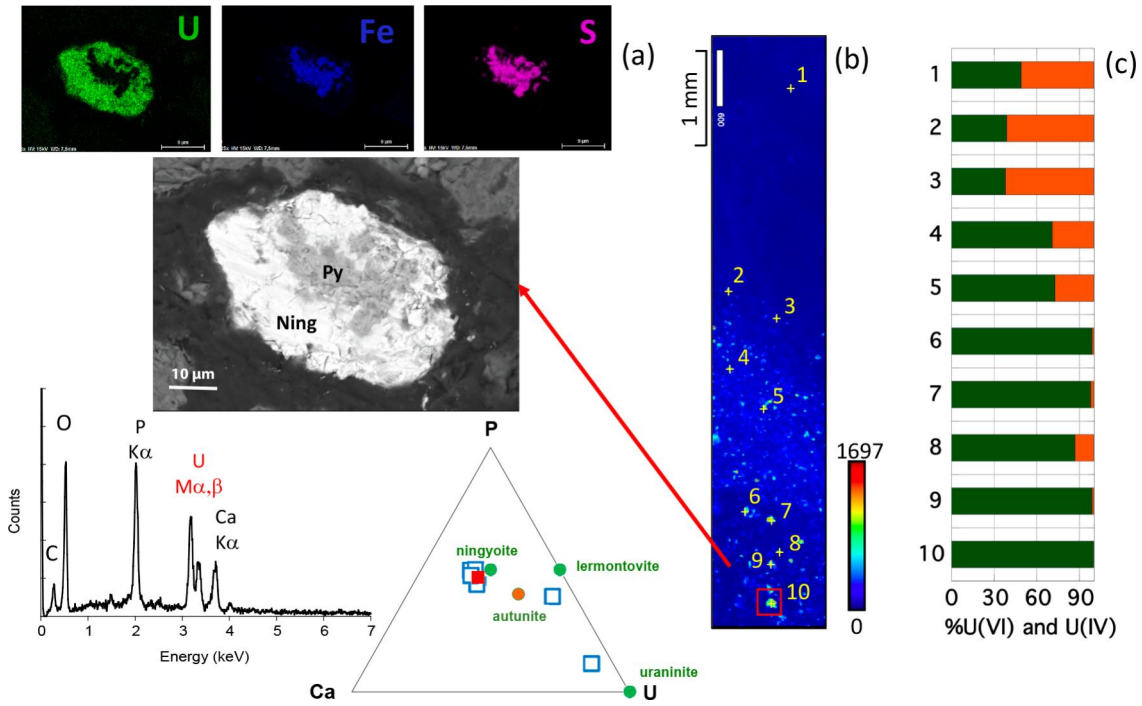

Figure 4. Microscale analysis of U-host mineral phases and U redox state at the U(VI)/U(IV) redox boundary in a polished section of the C6 core at 5−10 cm depth (see also Figure SI-7). (a) Backscattered electrons SEM image, elemental maps of U, Fe, and S and EDXS analysis (red square) of a U grain interpreted as ningyoite, corresponding to spot #10 of the μ-XRF elemental map; blue squares in the ternary diagram represents other U-mineral grains identified in the C2 and C6 cores, as detailed in the SI ; (b) μ-XRF elemental map (6.4 × 1.2 mm^2) showing the interface between the upper organic-rich layer A_1 and a mine water deposit layer with U-bearing grains. The number of counts on the U Lα line increases from blue to red on the color scale; and (c) U oxidation state determined by LCF fit of the μ-XANES spectra collected on spots 1 to 10 in the XRF map. The normalized proportions of U(VI) and U(IV) are displayed in orange and green color, respectively. Non-normalized results and uncertainties are given in Table SI-5. Ning: ningyoite, Py: pyrite.

SI-3) that was interpreted as a mixture between an organic-poor soil layer and mine water deposits (Figures 1 and SI-2a; Table SI-1). In our EXAFS-LCF procedure, the U(IV)-rhabdophane model compound $(Ca_{0.01}U_{0.01}La_{0.98})PO_4{\cdot}H_2O$ was used as a proxy for the isostructural mineral ningyoite $CaU(PO_4)_2{\cdot}2H_2O$ that was identified by SEM-EDXS analysis as an abundant U-host phase in these samples, as illustrated in Figure 4 for sample C6−10 cm. The local structure around U^{4+} ions in our $(Ca_{0.01}U_{0.01}La_{0.98})PO_4{\cdot}H_2O$ rhabdophane model compound was consistent with that expected in the rhabdophane/ningyoite structure, with characteristic U−P paths at 3.1 and 3.7 Å as well as U−Ca/La paths at 4.1 Å,[24] as confirmed by shell-by-shell fitting (Figure 3 ; Table SI-4). Another U(IV) phosphate mineral almost devoid of calcium was also observed in the mine water deposits below the U-redox boundary and was interpreted as lermontovite $U(PO_4)(OH){\cdot}H_2O$, vyacheslavite $U(PO_4)(OH){\cdot}2.5H_2O$ or Ca-depleted autunite $Ca(UO_2)_2(PO_4)_2{\cdot}11H_2O$ (Figure SI-8b), that have been discovered in weathered zones of hydrothermal uranium deposits.[56] According to these authors,[56] the crystal structures of vyacheslavite and especially of lermontovite have not been yet fully determined, which makes it difficult to evaluate their contribution to the EXAFS spectra in our soil samples. Besides, a unique grain of uraninite was also observed in the investigated samples (Figure SI-10a) but the contribution of this component to LCF was systematically found to be below 1%. Interestingly, ningyoite $CaU(PO_4)_2{\cdot}2H_2O$ was often found to be associated with massive pyrite grains in the C6−10 cm sample (Figure 4; Figure SI-9). Such observations could be interpreted as resulting from U(VI) reduction at the surface of pyrite.[57−59] Consistently, ningyoite or coffinite association with framboidal pyrite have been recently reported to be typical of (early)-diagenetic sedimentary uranium ore deposits,[60,61] while pitchblende is often associated with massive pyrite in meta-sedimentary[62,63] and hydrothermal[64] uranium ore deposits. To this regard, ningyoite associated with massive pyrite crystals and large lermontovite crystals found in the contaminated wetland soil studied could likely originate from epigenic zones of the Ty Gallen ore deposit that may be of hydrothermal origin.[65,66]

Uranium Speciation within the Water Table Fluctuation Zone. For the slightly oxidized sample C2−15 cm that was interpreted as an organic-poor mine water deposit sample located at the U-redox boundary, the best fit was obtained with 15% of autunite, 55% of U(IV)-rhabdophane and 40% of U(IV)-humus model (Figures 1, 2, and SI-2a, Tables SI-2 and SI-3). The proportion of U-phosphate minerals was lower (36%) in the slightly oxidized C2−25 cm sample (Figures 1 and 2), which corresponded to an organic-rich A1 soil layer contaminated by mine water deposit (Table SI-1; Figure SI-2a). In the C2−10 cm sample identified as a mine water deposits sample located just above the redox boundary of the C2 core, uranium was fully oxidized (Figure 1) and was under the form of mononuclear U(VI) species bound to organic matter/biomass (Figure 2). Indeed, best LCF fit were obtained with 35% U(VI)-humic acid and 66% U(VI)-biosorbed sample (Table SI-3). Adding autunite as a third fitting component did not improve the fit and yielded less than 10% for this component. This result indicated that U(IV)-phosphate minerals that might have been initially present in this mine water

deposit layer, as suggested by the presence of ningyoite in deeper samples, could have been oxidized and dissolved. One may thus infer that a fraction of the released U(VI) could have been scavenged by organic matter that occurs in mixture with this layer (9.8% TC; Table SI-1). Such a hypothetical process could help explain the exceptionally high concentrations of U under the form of U(VI)-organic complexes that we observed in the upper organic-rich layers, in both the C2 and C6 cores.

Finally, the EXAFS spectrum of the C6−5 cm sample was fit with 17% of U(VI)-biosorbed model compound and 76% of U(IV)-humus (Figure 2, Table SI-3) model compound that was obtained by experimental incubation of the C2−0 cm humus sample (see SI). We thus inferred that the abundance of such U(IV)-humus species in the C6−5 cm layer located just beneath the water table could have resulted from the reduction of a contaminated organic-rich layer of the A1-type similar to the overlying C6−0 cm layer, after a rise of the water table. Shell-by shell analysis of the U(IV)-humus data indicated a U−P paths at 3.1 Å and a U−C path at 3.7 Å (Figure 3, Table SI-4), which could be interpreted as bidentate and monodentate binding to phosphoryl and carboxyl groups, respectively. It thus appears that during the reduction of our U(VI)-humus samples, U(VI)-PO_4 monodentate complexes evolved toward U(IV)-PO_4 bidentate complexes, which is consistent with local environment of U(IV) and U(VI) in phosphate minerals and in mononuclear complexes, as discussed in previous studies.[24,43] In contrast, both U(VI) and U(IV) were mainly bound to carboxyl groups through mononuclear−monodentate complexes in our contaminated humus and organic rich soils samples, with a characteristic U−C distance at 3.3−3.4 Å (Figure 3; Table SI-4).

Implications for U Mobility in Contaminated Wetlands. The large contribution of U(IV)-phosphate minerals, especially ningyoite, to uranium speciation in the studied contaminated wetland soil raises issues on both the origin and the fate of such U(IV) minerals in contaminated environments. A few laboratory studies have reported the formation of ningyoite-like minerals via the bioreduction of poorly crystalline uranyl phosphate minerals[67,−69] or via biostimulation by glycerol phosphate under anaerobic conditions.[17] Accordingly, one could infer that U(IV)-phosphates observed in the Ty Gallen contaminated wetland soil could originate from the reduction of aqueous U(VI) species or of U(VI)-phosphate minerals, under reducing conditions that typically establish below the water table level in wetland soils. Such reduction processes could have been locally enhanced by the presence of reducing environments around massive pyrite crystals likely inherited from the Ty Gallen ore deposit. The presence of fine-grained ningyoite in the investigated soil (Figure 4; Figures SI-8a and 10b) would also support such a hypothesis. However, ningyoite coating on massive pyrite grains (Figures 4 and SI-9) together with large lermontovite/vyacheslavite/autunite grains (Figure SI-8b) and rare uraninite grains (Figure SI-10a) occurred only in mine water deposit layers characterized by abundant smectite component (Figure SI-2a), which rather suggests that these U(IV) minerals are inherited from the uranium ore and were transported to the wetland by mine water discharges.

Massive accumulation of U(VI) (1000−4500 mg/kg) was observed in organic-rich surface layers located at and above the water table redox boundary, under the form of uranyl monodentate complexes bound to carboxyl and phosphoryl groups of humic substances and microbial biomass (Figures 2 and 3). Such an association of uranyl with organic matter is consistent with previous studies of U speciation in naturally U-rich peatlands and contaminated wetland soils.[35,37,38] In the present study, given that U redox state rather depend on the water table level (Figure 1) than on the nature of U host phases (Figure 2), we propose that such uranium accumulation is due to organic complexation of U(VI) released by oxidative dissolution of U(IV)-phosphate minerals at and above the water table redox boundary. This explanation is especially supported by the presence of minute amount of U(VI)-phosphate minerals in the mine water deposit layer located at the water table redox boundary and its disappearing to the benefit of U(VI)-organic complexes just above this redox boundary, i.e., C2−15 cm and C2−10 cm sample in Figure 2. Such U remobilization due to water table fluctuations is consistent with the results of Gilson et al. 2015 that showed U redistribution during a short drying and rewetting period in sandy wetland mesocosms. Such redistribution may have proceeded vertically and also laterally due to underground and surface water flow in the wetland.

The significant complexation of U(IV) by organic matter observed in all the samples below the water table redox boundary (Figure 2) likely result from the reduction of U(VI)-humus material, as illustrated by the C6−5 cm sample. The presence of U(IV)-humus material in the deepest mine water deposit layers suggests past uranium redistribution before these layers were covered by more recent soil deposits. In contrast, it is important to note that the humus O, organic rich A1 and organic poor A2 soil layers located far below the present water table are devoided of uranium contamination, i.e., samples C2−35/40/45 cm and C6−20/25/30/cm in Figure 2. This result strongly suggests that in the carbonate-free environment studied here, U was not remobilized from the U(IV)-phosphate minerals and U(IV)-humate complexes out from these deep layers. Thus, permanent waterlogging would have ensured reducing conditions, potentially leading to long-term U scavenging.

In summary, our study yields evidence for major redistribution of uranium via oxidative dissolution of U(IV)-phosphate minerals at and above the water table, and subsequent reduction of U(VI) to U(IV)-organic complexes below the uranium redox boundary. To this regard, our results call for evaluating the kinetic of such oxidation−reduction reactions, with respect to water table fluctuation. Further research is therefore needed to evaluate *in situ* and *ex situ* the reactivity of U(IV) phosphates and mononuclear species in order to predict U mobility in such environments as a function of seasonal hydrological fluctuations.

(Figure SI-8,9 and 10); and VIII. Additional references cited (PDF)

AUTHOR INFORMATION

Corresponding Author

*E-mail: guillaume.morin@upmc.fr.

ORCID

Arnaud Mangeret: 0000-0002-2629-0400

John R. Bargar: 0000-0001-9303-4901

Guillaume Morin: 0000-0001-9304-4202

Notes

The authors declare no competing financial interest.

ACKNOWLEDGMENTS

Jean-Claude Boulliard is greatly acknowledged for having supplied mineral species samples from the IMPMC mineralogy collection. We are indebted to Imène Estève and Beatrice Doisneau for their help in the correlation of SEM-EDXS analyses with μ-XRF maps. We also acknowledge Ludovic Delbes for his help in XRD measurements and Rozimina Ibrahim for her help in samples preparation. We also thank Ms. Moizan the site's owner for the access to the field. The authors thank Jean-Louis Hazemann for his help on the FAME-CRG beamline at ESRF and Ryan Davis for his help during measurements at the 11-2 SSRL Beamline. A portion of this research was carried out at the Stanford Synchrotron Radiation Light Source, a national user facility operated by Stanford University, and on behalf of the US DOE Office of Basic Energy Sciences. This study was conducted within the framework of the IRSN/IMPMC collaborative research program number LS 20218/C151903-P150778. L.S.'s PhD has been granted by Region Ile de France, DIM R2DS PhD grant number 2015-03.

■ REFERENCES

(1) Pulford, I. D. Gold and uranium. In *Trace Elements in Soils*; Hooda, P. S., Ed.; Blackwell Publishing, Ltd., 2010; pp 551−565.

(2) Ielsch, G.; Cuney, M.; Buscail, F.; Rossi, F.; Leon, F.; Cushing, M. E. Estimation and mapping of uranium content of geological units in France. *J. Environ. Radioact.* **2017**, *166*, 210−219.

(3) Landa, E. R.; Gray, J. R. U.S. Geological Survey-Research on the environmental fate of uranium mining and milling wastes. *Environ. Geol.* **1995**, *26*, 19−31.

(4) Mangeret, A.; Blanchart, P.; Alcalde, G.; Amet, X.; Cazala, C.; Gallerand, M. O. An evidence of chemically and physically mediated migration of ^{238}U and its daughter isotopes in the vicinity of a former uranium mine. *J. Environ. Radioact.* **2018**, *195*, 67−71.

(5) Langmuir, D. *Aqueous Environmental Geochemistry*; Prentice Hall: Upper Saddle River, NJ, 1997.

(6) Newsome, L.; Morris, K.; Lloyd, J. R. The biogeochemistry and bioremediation of uranium and other priority radionuclides. *Chem. Geol.* **2014**, *363*, 164−184.

(7) Langmuir, D. Uranium solution-mineral equilibria at low-temperatures with applications to sedimentary ore-deposits. *Geochim. Cosmochim. Acta* **1978**, *42*, 547−569.

(8) Stewart, B. D.; Mayes, M. A.; Fendorf, S. Impact of Uranyl-Calcium-Carbonato Complexes on uranium(VI) adsorption to synthetic and natural sediments. *Environ. Sci. Technol.* **2010**, *44*, 928−934.

(9) Bednar, A. J.; Medina, V. F.; Ulmer-Scholle, D. S.; Frey, B. A.; Johnson, B. L.; Brostoff, W. N.; Larson, S. L. Effects of organic matter on the distribution of uranium in soil and plant matrices. *Chemosphere* **2007**, *70*, 237−247.

(10) Lovley, D. R.; Phillips, E. J. P.; Gorby, Y. A.; Landa, E. R. Microbial reduction of uranium. *Nature* **1991**, *350*, 413−416.

(11) Bargar, J. R.; Bernier-Latmani, R.; Giammar, D. E.; Tebo, B. M. Biogenic uraninite nanoparticles and their importance for uranium remediation. *Elements* **2008**, *4*, 407−412.

(12) Suzuki, Y.; Kelly, S. D.; Kemner, K. A.; Banfield, J. F. Direct microbial reduction and subsequent preservation of uranium in natural near-surface sediment. *Appl. Environ. Microbiol.* **2005**, *71*, 1790−1797.

(13) Hua, B.; Xu, H.; Terry, J.; Deng, B. Kinetics of uranium(VI) reduction by hydrogen sulfide in anoxic aqueous systems. *Environ. Sci. Technol.* **2006**, *40*, 4666−4671.

(14) Behrends, T.; Van Cappellen, P. Competition between enzymatic and abiotic reduction of uranium(VI) under iron reducing conditions. *Chem. Geol.* **2005**, *220*, 315−327.

(15) Veeramani, H.; Alessi, D.; Suvorova, E.; Lezama-Pacheco, J.; Stubbs, J.; Dippon, U.; Kappler, A.; Bargar, J.; Bernier-Latmani, R.; Sharp, J. O. Products of Abiotic U(VI) Reduction by Biogenic Magnetite and Vivianite. *Geochim. Cosmochim. Acta* **2011**, *75*, 2512−2528.

(16) Sharp, J. O.; Schofield, E. J.; Veeramani, H.; Suvorova, E. I.; Kennedy, D. W.; Marshall, M. J.; Mehta, A.; Bargar, J. R.; Bernier-Latmani, R. Structural similarities between biogenic uraninites produced by phylogenetically and metabollically diverse bacteria. *Environ. Sci. Technol.* **2009**, *43*, 8295−8301.

(17) Newsome, L.; Morris, K.; Trivedi, D.; Bewsher, A.; Lloyd, J. R. Biostimulation by Glycerol Phosphate to Precipitate Recalcitrant Uranium(IV) Phosphate. *Environ. Sci. Technol.* **2015**, *49*, 11070−11078.

(18) Bernier-Latmani, R.; Veeramani, H.; Vecchia, E. D.; Junier, P.; Lezama-Pacheco, J. S.; Suvorova, E. I.; Sharp, J. O.; Wigginton, N. S.; Bargar, J. R. Non-uraninite products of microbial U(VI) reduction. *Environ. Sci. Technol.* **2010**, *44*, 9456−9462.

(19) Fletcher, K. E.; Boyanov, M. I.; Thomas, S. H.; Wu, Q.; Kemner, K. M.; Löffler, F. E. U(VI) reduction to mononuclear U(IV) by *Desulfitobacterium* species. *Environ. Sci. Technol.* **2010**, *44*, 4705−4709.

(20) Boyanov, M. I.; Fletcher, K. E.; Kwon, M. J.; Rui, X.; O'Loughlin, E. J.; Löffler, F. E.; Kemner, K. M. Solution and microbial controls on the formation of reduced U(IV) phases. *Environ. Sci. Technol.* **2011**, *45*, 8336−8344.

(21) Wang, Y.; Frutschi, M.; Suvorova, E.; Phrommavanh, V.; Descostes, M.; Osman, A. A. A.; Geipel, G.; Bernier-Latmani, R. Mobile uranium(IV)-bearing colloids in a mining impacted wetland. *Nat. Commun.* **2013**, *4*, 2942.

(22) Bargar, J. R.; Williams, K. H.; Campbell, K. M.; Long, P. E.; Stubbs, J. E.; Suvorova, E. I.; Lezama- Pacheco, J. S.; Alessi, D. S.; Stylo, M.; Webb, S. M.; Davis, J. A.; Giammar, D. E.; Blue, L. Y.; Bernier-Latmani, R. Uranium redox transition pathways in acetate-amended sediments. *Proc. Natl. Acad. Sci. U. S. A.* **2013**, *110*, 4506−4511.

(23) Bhattacharyya, A.; Campbell, K. M.; Kelly, S. D.; Roebbert, Y.; Weyer, S.; Bernier-Latmani, R.; Borch, T. Biogenic non-crystalline U (IV) revealed as major component in uranium ore deposits. *Nat. Commun.* **2017**, *8*, 15538.

(24) Morin, G.; Mangeret, A.; Othmane, G.; Stetten, L.; Seder-Colomina, M.; Brest, J.; Ona-Nguema, G.; Bassot, S.; Courbet, C.; Guillevic, J.; Thouvenot, A.; Mathon, O.; Proux, O.; Bargar, J. R. Mononuclear U(IV) complexes and ningyoite as major uranium species in lake sediments. *Geochemical Perspectives Letters* **2016**, *2*, 95−105.

(25) Stetten, L.; Mangeret, A.; Brest, J.; Seder-Colomina, M.; Le Pape, P.; Ikogou, M.; Zeyen, N.; Thouvenot, A.; Julien, A.; Alcalde, G.; Reyss, J. L.; Bombled, B.; Rabouille, C.; Olivi, L.; Proux, O.; Cazala, C.; Morin, G. Geochemical control on the reduction of U(VI) to mononuclear U(IV) species in a contaminated lake sediment. *Geochim. Cosmochim. Acta* **2018**, *222*, 171−186.

(26) Cerrato, J. M.; Ashner, M. N.; Alessi, D. S.; Lezama-Pacheco, J. S.; Bernier-Latmani, R.; Bargar, J. R.; Giammar, D. E. Relative

reactivity of biogenic and chemogenic uraninite and biogenic noncrystalline U(IV). *Environ. Sci. Technol.* **2013**, *47*, 9756−9763.
(27) Noller, B. N.; Woods, P. H.; Ross, B. J. Case-studies of wetland filtration of mine waste-water in constructed and naturally-occurring systems in Northern Australia. *Water Sci. Technol.* **1994**, *29*, 257−265.
(28) Owen, D. E.; Otton, J. K. Mountain wetlands: efficient uranium filters - potential impacts. *Ecological Engineering* **1995**, *5*, 77−93.
(29) Schöner, A.; Noubactep, C.; Büchel, G.; Sauter, M. Geochemistry of natural wetlands in former uranium milling sites (eastern Germany) and implications for uranium retention. *Chem. Erde* **2009**, *69*, 91−107.
(30) Schöner, A.; Noubactep, C.; Sauter, M. Assessment of uranium retention in wetlands: Characterisation of bonding strength, considerations to optimize reductive precipitation. IMWA Symposium—Mine Water 2004—Process, Policy and Progress, Vol. (ISBN 0-9543827-4-9); University of Newcastle upon Tyne: Newcastle, U.K., 2004, *2*, 19−24.
(31) Couture, R.-M.; Charlet, L.; Markelova, E.; Madé, B.; Parsons, C. T. On−Off Mobilization of Contaminants in Soils during Redox Oscillations. *Environ. Sci. Technol.* **2015**, *49*, 3015−3023.
(32) Kaplan, D. I.; Buettner, S. W.; Li, D.; Huang, S.; Koster van Groos, P. G.; Jaffé, P. R.; Seaman, J. C. *In situ* porewater uranium concentrations in a contaminated wetland: Effect of seasons and sediment depth. *Appl. Geochem.* **2017**, *85*, 128−136.
(33) Noël, V.; Boye, K.; Lezama Pacheco, J. S.; Bone, S. E.; Janot, N.; Cardarelli, E.; Williams, K. H.; Bargar, J. R. Redox Controls over the Stability of U(IV) in Floodplains of the Upper Colorado River Basin. *Environ. Sci. Technol.* **2017**, *51*, 10954−10964.
(34) Schumann, R. R.; Zielinski, R. A.; Otton, J. K.; Pantea, M. P.; Orem, W. H. Uranium delivery and uptake in a montane wetland, north-central Colorado, USA. *Appl. Geochem.* **2017**, *78*, 363−379.
(35) Regenspurg, S.; Margot-Roquier, C.; Harfouche, M.; Froidevaux, P.; Steinmann, P.; Junier, P.; Bernier-Latmani, R. Speciation of naturally-accumulated uranium in an organic-rich soil of an alpine region (Switzerland). *Geochim. Cosmochim. Acta* **2010**, *74*, 2082−2098.
(36) Kaplan, D.; Kukkadapu, R.; Seaman, J. C.; Arey, B. W.; Dohnalkova, A. C.; Buettner, S.; Li, D.; Varga, T.; Scheckel, K. G.; Jaffé, P. R. Iron mineralogy and uranium-binding environment in the rhizosphere of a wetland soil. *Sci. Total Environ.* **2016**, *569*−*570*, 53−64.
(37) Li, D.; Kaplan, D. I.; Chang, H.-S.; Seaman, J. C.; Jaffé, P. R.; Koster van Groos, P.; Scheckel, K. G.; Segre, C. U.; Chen, N.; Jiang, D.-T.; Newville, M.; Lanzirotti, A. Spectroscopic evidence of uranium immobilization in acidic wetlands by natural organic matter and plant roots. *Environ. Sci. Technol.* **2015**, *49*, 2823−2832.
(38) Mikutta, C.; Langner, P.; Bargar, J. R.; Kretzschmar, R. Tetra- and Hexavalent uranium forms bidendate- mononuclear complexes with particulate organic matter in a naturally uranium- enriched peatland. *Environ. Sci. Technol.* **2016**, *50*, 10465−10475.
(39) Wang, Y.; Bagnoud, A.; Suvorova, E.; McGivney, E.; Chesaux, L.; Phrommavanh, V.; Descostes, M.; Bernier-Latmani, R. Geochemical control on uranium(IV) mobility in a mining-impacted wetland. *Environ. Sci. Technol.* **2014**, *48*, 10062−10070.
(40) Proux, O.; Biquard, X.; Lahera, E.; Menthonnex, J.-J.; Prat, A.; Ulrich, O.; Soldo, Y.; Trvisson, P.; Kapoujyan, G.; Perroux, G.; Taunier, P.; Grand, D.; Jeantet, P.; Deleglise, M.; Roux, J.-P.; Hazemann, J.-L. FAME: a new beamline for X-ray absorption investigations of very-diluted systems of environmental, material and biological interests. *Phys. Scr.* **2005**, *115*, 970−973.
(41) Webb, S. M. SIXpack: a graphical user interface for XAS analysis using IFEFFIT. *Phys. Scr.* **2005**, *T115*, 1011−1014.
(42) Ravel, B.; Newville, M. ATHENA, ARTEMIS, HEPHAESTUS: data analysis for X-ray absorption spectroscopy using IFEFFIT. *J. Synchrotron Radiat.* **2005**, *12*, 537−541.
(43) Seder-Colomina, M.; Morin, G.; Brest, J.; Ona-Nguema, G.; Gordien, N.; Pernelle, J.-J.; Banerjee, D.; Mathon, O.; Esposito, G.; van Hullebusch, E. D. Uranium(VI) Scavenging by Amorphous Iron Phosphate Encrusting Sphaerotilus natans Filaments. *Environ. Sci. Technol.* **2015**, *49*, 14065−14075.
(44) Ankudinov, A. L.; Ravel, B.; Rehr, J. J.; Conradson, S. D. Real-space multiple-scattering calculation and interpretation of x-ray-absorption near-edge structure. *Phys. Rev. B: Condens. Matter Mater. Phys.* **1998**, *58*, 7565−7576.
(45) Locock, A. J.; Burns, P. C. Crystal structures and synthesis of the copper-dominant members of the autunite and meta-autunite groups: torbernite, zeunerite, metatorbernite and metazeunerite. *Can. Mineral.* **2003**, *41*, 489−502.
(46) Dusausoy, Y.; Ghermani, N. E.; Podor, R.; Cuney, M. Low-temperature ordered phase of $CaU(PO_4)_2$: synthesis and crystal structure. *Eur. J. Mineral.* **1996**, *8*, 667−673.
(47) Howatson, J.; Grev, D. M.; Morosin, B. Crystal and molecular structure of uranyl acetate dihydrate. *J. Inorg. Nucl. Chem.* **1975**, *37*, 1933−1935.
(48) Othmane, G.; Allard, T.; Morin, G.; Sélo, M.; Llorens, I.; Chen, H.; Bargar, J.; Fayek, M.; Calas, G.; Brest, J. Uranium association with iron-bearing phases in mill tailings from Gunnar, Canada. *Environ. Sci. Technol.* **2013**, *47*, 12695−12702.
(49) Cornell, R. M., Schwertmann, U. *the Iron Oxides: Structure, Properties, Reactions, Occurrences and Uses*; Wiley-VCH: Weinheim, 2003.
(50) Schlosser, F.; Krüger, S.; Rösch, N. A Density Functional Study of Uranyl Monocarboxylates. *Inorg. Chem.* **2006**, *45*, 1480−1490.
(51) Denecke, M. A.; Reich, T.; Bubner, M.; Pompe, S.; Heise, K. H.; Nitsche, H.; Allen, P. G.; Bucher, J. J.; Edelstein, N. M.; Shuh, D. K. Determination of structural parameters of uranyl ions complexed with organic acids using EXAFS. *J. Alloys Compd.* **1998**, *271*−*273*, 123−127.
(52) Schmeide, K.; Sachs, S.; Bubner, M.; Reich, T.; Heise, K. H.; Bernhard, G. Interaction of uranium(VI) with various modified and unmodified natural and synthetic humic substances studied by EXAFS and FTIR spectroscopy. *Inorg. Chim. Acta* **2003**, *351*, 133−140.
(53) Bargar, J. R.; Reitmeyer, R.; Lenhart, J. J.; Davis, J. A. Characterization of U(VI)-carbonato ternary complexes on hematite: EXAFS and electrophoretic mobility measurements. *Geochim. Cosmochim. Acta* **2000**, *64*, 2737−2749.
(54) Rossberg, A.; Ulrich, K.-U.; Weiss, S.; Tsushima, S.; Hiemstra, T.; Scheinost, A. C. Identification of uranyl surface complexes on ferrihydrite: Advanced EXAFS data analysis and CD-MUSIC modeling. *Environ. Sci. Technol.* **2009**, *43*, 1400−1406.
(55) Kelly, S. D.; Kemner, K. M.; Fein, J. B.; Fowle, D. A.; Boyanov, M. I.; Bunker, B. A.; Yee, N. X-ray absorption fine structure determination of pH-dependent U-bacterial cell wall interactions. *Geochim. Cosmochim. Acta* **2002**, *66*, 3855−3871.
(56) Krivovichev, S. V.; Plášil, J. Mineralogy and Crystallography of Uranium. In: *Uranium: From Cradle to Grave*; Burns, P. C., Sigmon, G. E., Eds. Mineralogical Association of Canada Short Courses 43: Winnipeg MB, May 2013, pp. 15−119.
(57) Wersin, P.; Hochella, M. F.; Persson, P.; Redden, G.; Leckie, J. O.; Harris, D. W. Interaction between aqueous uranium(VI) and sulfide minerals − spectroscopic evidence for sorption and reduction. *Geochim. Cosmochim. Acta* **1994**, *58*, 2829−2843.
(58) Scott, T. B.; Riba Tort, O.; Allen, G. C. Aqueous uptake of uranium onto pyrite surfaces; reactivity of fresh versus weathered material. *Geochim. Cosmochim. Acta* **2007**, *71*, 5044−5053.
(59) Descostes, M.; Schlegel, M. L.; Eglizaud, N.; Descamps, F.; Miserque, F.; Simoni, E. Uptake of uranium and trace elements in pyrite (FeS2) suspensions. *Geochim. Cosmochim. Acta* **2010**, *74*, 1551−1562.
(60) Doynikova, O. A.; Tarasov, N. N.; Mokhov, A. V. A New Phosphatic Type of Uranium Deposits in Russia. *Dokl. Earth Sci.* **2014**, *457*, 910−914.
(61) Bonnetti, C.; Cuney, M.; Malartre, F.; Michels, R.; Liu, X.; Peng, Y. The Nuheting deposit, Erlian Basin, NE China: Synsedimentary to diagenetic uranium mineralization. *Ore Geol. Rev.* **2015**, *69*, 118−139.

(62) Simpson, P. R.; Bowles, J. F. W. Uranium mineralisation in the Witwatersrand and Dominion reef systems. *Philos. Trans. R. Soc., A* **1977**, *286*, 527−548.
(63) England, G. L.; Rasmussen, B.; Krapez, B.; Groves, D. I. The origin of uraninite, bitumen nodules and carbon seams in the Witwatersrand gold−uranium−pyrite ore deposits, based on a Permo-Triassic analogue. *Econ. Geol. Bull. Soc. Econ. Geol.* **2001**, *96*, 1907−1920.
(64) Cunningham, C. G.; Rasmussen, J. D.; Steven, T. A.; Rye, R. O.; Rowley, P. D.; Romberger, S. B.; Selverstone, J. Hydrothermal uranium deposits containing molybdenum and fluorite in the Marysvale volcanic field, west-central Utah. *Miner. Deposita* **1998**, *33*, 477−494.
(65) Gaines, R. V.; Skinner, H. C. W.; Foord, E. E.; Mason, B.; Rosenzweig, A.; King, V. T.; Dowty, E. *Dana's New Mineralogy*, 8th ed.; Wiley & Sons: New-York, 1997; p 1819.
(66) Finch, R.; Murakami, T. Systematics and paragenesis of uranium minerals. In *Uranium: Mineralogy, Geochemistry and the Environment*; Burns, P. C., Finch, R., Eds.; Mineralogical Society of America: Washington, DC, 1999; Vol. *38*, pp 91−179.
(67) Khijniak, T. V.; Slobodkin, A. I.; Coker, V.; Renshaw, J. C.; Livens, F. R.; Bonch-Osmolovskaya, E. A.; Birkeland, N.-K.; Medvedeva-Lyalikova, N. N.; Lloyd, J. R. Reduction of Uranium(VI) Phosphate during Growth of the Thermophilic Bacterium Thermoterrabacterium ferrireducens. *Applied and environmental microbiology* **2005**, *71*, 6423−6426.
(68) Rui, X.; Kwon, M. J.; O'Loughlin, E. J.; Dunham-Cheatham, S.; Fein, J. B.; Bunker, B.; Kemner, K. M.; Boyanov, M. I. Bioreduction of Hydrogen Uranyl Phosphate: Mechanisms and U(IV) Products. *Environ. Sci. Technol.* **2013**, *47*, 5668−5678.
(69) Gilson, E. R.; Huang, S.; Koster van Groos, P. G.; Scheckel, K. G.; Qafoku, O.; Peacock, A. D.; Kaplan, D. I.; Jaffe, P. R. Uranium Redistribution Due to Water Table Fluctuations in Sandy Wetland Mesocosms. *Environ. Sci. Technol.* **2015**, *49*, 12214−12222.